

Effect of Annealing on Electronic Transport in Modulation-doped $\text{In}_{0.32}\text{Ga}_{0.68}\text{As}/\text{GaAs}$ Quantum Well Structures

A. Rajhi^{1,2} , M. Aydın^{1*} , Ö. Dönmez¹ , F. Sarcan¹ , and A. Erol¹ 

¹Istanbul University, Faculty of Science, Department of Physics, Vezneciler, 34134, İstanbul, Türkiye

²Al Zaytouna University, Faculty of Science, Department of Physics, Asalam, 325, Tarhuna, Libya

ABSTRACT

In this study, electronic transport properties of n-type modulation-doped $\text{In}_{0.32}\text{Ga}_{0.68}\text{As}/\text{GaAs}$ quantum well (QW) quasi 2D structures and the effects of post-growth rapid thermal annealing and growth temperature are determined. Electron Hall mobility and carrier concentration of $\text{In}_{0.32}\text{Ga}_{0.68}\text{As}/\text{GaAs}$ QW were determined using the Hall effect measurement at a temperature range between 4.2 K and 300 K. While the low-temperature electron mobility has temperature-independent behavior, electron mobility at high-temperatures deteriorates drastically. However, for low-temperature growth samples, electron mobility shows a slight increase at lower temperatures. The effects of annealing and growth temperature on electronic transport properties are investigated and compared in terms of carrier mobility, carried density, effective mass and scattering mechanisms. To determine the dominant scattering mechanisms in the 2D structures of $\text{In}_{0.32}\text{Ga}_{0.68}\text{As}/\text{GaAs}$, temperature-dependent Hall mobility results are fitted using an analytical model, considering all possible scattering mechanisms (interface roughness, alloy disorder, acoustic phonon, polar optical phonon and remote ionized impurity scattering) in the 2D samples. Magnetotransport (MR) measurements were carried out between 4.2 K and 50 K and the effective mass, Fermi level, and 2D carrier density were calculated by analyzing amplitudes of temperature dependence Shubnikov de Haas (SdH) oscillations. Our results indicate that the effects of annealing at 700°C-600s reduce interface roughness and alloy disorder scattering, thereby enhancing electron mobility. Post-growth thermal annealing improved electron mobility. Also, annealing increases the effect mass and causes a reduction in the electron concentrations of the $\text{InGaAs}/\text{GaAs}$ QW systems. Additionally, thermal annealing increases the effective electron mass while decreasing electron concentration.

Keywords: $\text{In}_{0.32}\text{Ga}_{0.68}\text{As}/\text{GaAs}$; 2D structures ; modulation doped structures ; electronic transport

1. INTRODUCTION

InGaAs alloy has been using in near-infrared applications as an active material for photodetectors and light emitters. The bandgap of the material can be tuned as a function of In concentration in the alloy. It has been shown in the literature that the band gap redshifts by 12 meV/In% (Petropoulos et al. 2011; Maspero et al. 2017; Lin et al. 2019). This tunability with In% concentration allows the desired bandgap in the active material for near-infrared optoelectronic device applications (Feng et al. 2005). Due to the increment in the lattice constant of alloy compared to GaAs host materials, substrate selection is critical (Matthews & Blakeslee 1974; Dahl 2002). While an InP substrate is suitable for the high In concentration, a GaAs substrate is suitable for the low In concentrations. InGaAs alloys grown by Molecular Beam Epitaxy (MBE) on GaAs require lower growth temperatures than those of growth on InP substrate to avoid defects, which cause poor electrical and optical properties such as low mobility, and low emission intensity (Mu-

raki et al. 1992; Toyoshima et al. 1993; Disseix et al. 1997). However, post-growth thermal annealing has been shown to have favorable effects on the electronic and optical properties of III-V group semiconductors (Ardali et al. 2021; Dönmez et al. 2020). Accordingly, rapid thermal annealing (RTA) provides a low-cost, simple, and powerful way to tune and improve the structural and optical qualities of nanostructures, such as bandgap energy, confinement, and absorption, and offers the potential to develop new types of devices and integrated optoelectronic circuits (Li et al. 2019). RTA is also used to reduce defects arising from low-growth temperatures by MBE (Kosogov et al. 1996). In a study on the effect of thermal annealing for InGaAs-GaAs strained-layer, it was shown that high temperature and prolonged thermal annealing have a significant effect on the diffusion coefficient (depending on annealing temperature, for 900°C it is about $8 \times 10^{-18} \text{cm}^2 \text{s}^{-1}$ and for 850°C it is about $8 \times 10^{-20} \text{cm}^2 \text{s}^{-1}$, respectively) (Kosogov et al. 1996; Joncour et al. 1985). It was reported that a blueshift occurred

Corresponding Author: M. Aydın **E-mail:** mustafaaydin@istanbul.edu.tr

Submitted: 05.10.2023 • **Accepted:** 19.12.2023 • **Published Online:** 05.06.2024



This article is licensed under a Creative Commons Attribution-NonCommercial 4.0 International License (CC BY-NC 4.0)

as the annealing time increased, attributed to the decrease in In alloy concentration. (Li et al. 2019; Aldridge et al. 2017; Kuphal 1984).

In this study, the effect of n-type modulation-doped thermal annealing at 700°C during 600 s on the electronic properties of In_{0.32}Ga_{0.68}As/GaAs quantum well (QW) structure grown at 475°C (TNL) and 580°C (TNH) was investigated. Hall Effect experiments between 4K and 300K were performed to analyze the electronic properties of n-type as-grown and annealed InGaAs/GaAs QWs grown at different temperatures. The results of Hall Effect experiments were analyzed taking into account the scattering mechanisms of interface roughness, alloy disorder, acoustic phonon, polar optical phonon and remote ionized impurity scatterings. MR experiments were performed between 4K and 50K. Shubnikov-de Haas (SdH) oscillations were observed in MR experiments. These oscillations were analyzed to determine the 2D carrier concentration, the position of the Fermi level, and the effective mass of all samples.

2. METHODS

2.1. Sample Growth and Fabrication

Samples were grown as reference examples to compare the electronic transport mechanism of the N-containing samples. For this reason, the growth process using Molecular Beam Epitaxy (MBE) was carried out at two different temperatures: the low temperature (475°C) at which the crystal quality of the nitrogen-containing structures obtained the best and the optimum temperature (580°C) of the GaAs-based samples. We have also studied the effect of growth temperature, investigated growth temperatures and the electronic transport mechanisms of the samples after thermal annealing. The samples were subjected to 600s thermal annealing at 700°C to investigate the effects of thermal annealing. The sample structure is illustrated in Figure 1. The samples were grown on a semi-insulating (SI) GaAs substrate that does not affect its electrical properties and acts as a passive substrate. The structure consists of an n-type doped GaAs barrier and undoped InGaAs layer that forms the QW. Si dopant concentration (N_D) was 10^{18}cm^{-3} . GaAs layers were grown at 580°C while the InGaAs layer forming QW was grown at 475°C for TNL and 580°C for TNH. Modulation doping was achieved by growing an undoped spacer GaAs layer with a thickness of 5nm between the doped barrier layer and the QW in order to spatially separate the carriers passing through the QW from the barrier, with their ionized parents in the barrier, and weaken the Coulomb interaction between them. The sample was then fabricated into a Hall Bar shape using a wet etching process. Hall bar dimensions are given in Figure 1b.

2.2. Theoretical Background: Analytic modeling of temperature dependence of electron mobility

This section will discuss several scattering mechanisms, such as acoustic phonon scattering (μ_{APH}), alloy disorder scattering (μ_{Alloy}), interface roughness scattering (μ_{IFR}), and remote

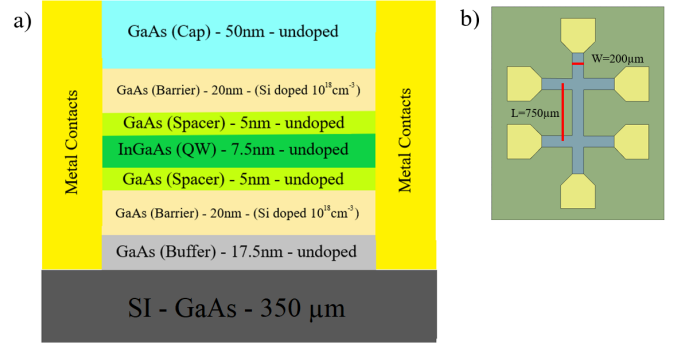


Figure 1. (a) Modulation-doped In_{0.32}Ga_{0.68}As/GaAs QW sample structure, (b) Fabricated Hall Bar shape and its dimensions.

impurity scattering (μ_{RI}), which play a significant role in determining carrier mobility in a semiconductor.

2.2.1. Interface Roughness Scattering

In layered structures like modulation-doped structures, interface roughness scattering is a crucial scattering mechanism due to imperfections at the interface between different materials. Because the sample is grown layer by layer, and the layers consist of different materials with different lattice constants and dielectric constants, roughness will occur at the interface between the layers, resulting in interface scattering. Interface roughness scattering mobility can be written as (Donmez et al. 2021, 2014),

$$\mu_{\text{IFR}} = \left(\frac{2\varepsilon_0\varepsilon_s}{n_{2D}\Delta\Lambda} \right)^2 \frac{\hbar^3}{e^3 m^*{}^2} \frac{1}{j_{\text{IFR}}(k)} \quad (1)$$

Here n_{2D} is the 2D carrier density, and Δ denotes the lateral size of the interface roughness, and Λ stands for the correlation length between fluctuations. The integral $J_{\text{IFR}}(k)$ is given by Zanato et al. (2004),

$$J_{\text{IFR}}(k) = \int_0^{2k} \frac{e^{-q^2\Lambda^2/4}}{2k^3(q + q_{2D})\sqrt{1 - (\frac{q}{2k})^2}} q^4 dq \quad (2)$$

where $q = 2 \sin(\theta/2)$, θ represents the scattering angle, and q_{2D} denotes the inverse screening length.

2.2.2. Alloy Disorder Scattering

Alloy fluctuation scattering is caused by potential fluctuations due to the random distribution of the atoms forming an alloy in the crystal. Alloy disorder scattering is given by

$$\mu_{\text{Alloy}} = \frac{16e\hbar^3}{3b_{\text{FH}} \times (1-x)m^*{}^2\Omega_0 U_{\text{Alloy}}^2} \quad (3)$$

where x is the alloy content, the primitive cell volume, Ω_0 , the effective mass of the carrier, m^* , for ternary alloys, the potential alloy, U_{Alloy} , and factor b_{FH} is the Fang-Howard expression (Donmez et al. 2021).

2.2.3. Acoustic Phonon Scattering

Acoustic phonons are divided into two branches: transverse and longitudinal acoustic phonons, depending on the transverse and longitudinal oscillations of atoms. The acoustic phonon scattering increases with temperature, because the density of phonons increases at higher temperature according to Bose-Einstein statistics. Acoustic phonon scattering includes deformation potential scattering and piezoelectric scattering.

Deformation Potential Scattering

The deformation potential limited mobility is defined by *Ridley* ([Zanato et al. 2004](#)) as

$$\mu_{DP} = \frac{16\rho e\vartheta_L^2\hbar^3}{3E_{DP}^2 k_B T m^{*2} b_{FH}} \frac{1}{j_{DP}(k)} \quad (4)$$

where ρ , E_{DP} , ϑ_L , b_{FH} are the crystal density, deformation potential, longitudinal acoustic phonon velocity and Fang-Howards expression, respectively. $J_{DP}(k)$ is given as

$$J_{DP}(k) = \int_0^{2k} \frac{1}{2\pi k^3 (q + q_{2D})^2 \sqrt{1 - (\frac{q}{2k})^2}} q^4 dq \quad (5)$$

Piezoelectric Scattering

The mobility limited by piezoelectric scattering is defined as ([Donmez et al. 2021, 2014](#)),

$$\mu_{PE} = \frac{\pi\varepsilon_0\varepsilon_s\hbar^3 k}{eK_{av}^2 k_B T m^{*2}} \frac{1}{j_{PE}(k)} \quad (6)$$

Here K_{av} is the average electromechanical coupling constant. $J_{PE}(k)$ is given as

$$J_{PE}(k) = \int_0^{2k} \frac{F(q)}{4k^2 (q + q_{2D})^2 \sqrt{1 - (\frac{q}{2k})^2}} q^3 dq \quad (7)$$

2.2.4. Polar Optical Phonon Scattering

Optical phonon scattering becomes more effective at higher temperatures. The mobility restricted by polar optical phonon scattering is expressed as ([Donmez et al. 2021, 2014](#)):

$$\mu_{PE} = \frac{4\pi\varepsilon_0\varepsilon_p\hbar^2}{e\omega_{PO}m^{*2}L} \left[\exp\left(\frac{\hbar\omega_{PO}}{k_B T}\right) - 1 \right] \quad (8)$$

where $\hbar\omega_{PO}$ is polar optical phonon energy and L quantum well width. ε_p is defined as

$$\varepsilon_p = \left[\frac{1}{\varepsilon_\infty} - \frac{1}{\varepsilon_s} \right]^{-1} \quad (9)$$

2.2.5. Remote Ionized Impurity Scattering

Remote ionized impurity scattering is caused by ionized doping atoms and is a Coulombic interaction between charge carriers in the QW and the ionized impurities in the barrier layer. Compared to the ionized impurity scattering, remote scattering is less effective in modulation-doped structures, where dopant atoms and carriers are spatially distant from each other, thus reducing scattering and improving electron mobility. The mobility limited by scattering of remote ionized impurity atoms is expressed as ([Donmez et al. 2021, 2014](#)),

$$\mu_{RI} = \left(\frac{64\pi\hbar\varepsilon_0 S_0^2 (2\pi n_{2D})^{3/2}}{e^3 m^*} \right)^2 \left[\frac{1}{L^2} - \frac{1}{(d_1 + L)^2} \right]^{-1} \quad (10)$$

where d_1 , L and S_0 are the spacer layer thickness, QW width and static constant, respectively. S_0 is defined as the screening constant ([Donmez et al. 2020, 2014](#)).

2.2.6. Matthiessen Rule

The effect of summing each kind of scattering center can be expressed with the assumption that each scattering mechanism is independent of each other, using the formula developed by Matthiessen as,

$$\frac{1}{\mu_{Total}} = \sum_i \frac{1}{\mu_i} \quad (11)$$

2.3. Theoretical Background: Analysis of Shubnikov-de Haas (SdH) Oscillations

In low-dimensional semiconductor systems, the energy difference between two subsequent Landau levels increases with the increasing magnetic field applied to the semiconductor in the growth direction. The Landau levels expand and approach the Fermi level, and if the magnetic field intensity is sufficient, the Landau levels pass through the Fermi level. As a result, oscillations occur at the density at the Fermi level, so the longitudinal resistivity (ρ_{xx}) oscillates. These oscillations are called Shubnikov-de Haas (SdH) oscillations.

$$\rho_{xx}(B) = \rho_{non-osc}(B) + \rho_{ocs}(B) \quad (12)$$

Experimental results provide the total of non-oscillating part and SdH oscillations. Considering that the effective mass and quantum lifetime can be different for each subband, the analytical expression for SdH oscillations is as follows ([Coleridge 1990; Balkan et al. 1995](#)):

$$\frac{\Delta\rho_{xx}}{\rho_0} \sim \sum_{i=1}^{\infty} D(i\chi) \exp\left(\frac{-i\pi}{\omega_c \tau_q}\right) \cos\left[\frac{2\pi(E_F - E_i)}{\hbar\omega_c} - i\pi\right] \quad (13)$$

where ρ_{xx} , ρ_0 , E_1 , E_F , ω_c and τ_q are oscillatory part of magnetoresistivity, magnetoresistivity, first sub-band energy, Fermi energy, cyclotron frequency and quantum lifetime, respectively.

i , represents the sub-bands. $\exp\left(\frac{-i\pi}{\omega_c \tau_q}\right)$ represents damping due to the broadening of the levels resulting from the collision of the Landau levels. $D(i\chi)$ describes the temperature damping as follows:

$$D(i\chi) = \frac{\chi}{\sinh \chi} \quad (14)$$

$$\chi = \frac{2\pi^2 k_B T}{\hbar \omega_c} \quad (15)$$

Assuming that the quantum lifetime of the electron is independent of temperature, the oscillation amplitude is expressed as

$$A(T, B_n) = C_1 \frac{2\pi^2 k_B T / \hbar \omega_c}{\sinh(2\pi^2 k_B T / \hbar \omega_c)} \quad (16)$$

where C_1 is constant. The ratio of the amplitudes of the oscillations at two different temperatures gives

$$\frac{A(T, B_n)}{A(T_0, B_n)} = \frac{T \sinh(2\pi^2 k_B T_0 m^* / \hbar \omega_c)}{T_0 \sinh(2\pi^2 k_B T m^* / \hbar \omega_c)} \quad (17)$$

The experimental data obtained for the variation of the relative amplitude with temperature are fitted to Equation 17 to obtain the effective mass with high accuracy. The position of the Fermi level and n_{2D} is also determined by Equation 18 using the slope of the inverse magnetic field plot versus the number of oscillation peaks.

$$\Delta_i \left(\frac{1}{B} \right) = \frac{e\hbar}{m^*(E_F - E_i)} = \frac{e}{\pi \hbar n_{2D}} \quad (18)$$

3. RESULTS

3.1. Low Magnetic Field Results

Hall measurements were conducted to determine carrier mobility and carrier concentration under a constant magnetic field in the temperature range of 4.2 to 300K.

Figure 2 a-b shows the temperature-dependent mobility and electron density of all samples. The temperature dependence of the electron mobility exhibits the well-known characteristic of modulation-doped structures. At low temperatures ($T < 77K$), electron mobility is almost the temperature-independent where ionized impurity scattering is dominant in conventional doped heterostructures. Thanks to the modulation doping, we observed that the mobility is very high for all samples at temperature lower than 77 K. The highest mobility ($43121 \text{ cm}^2 \text{ V}_s^{-1}$) for as-grown samples are observed for TNL at low temperatures ($T < 100K$) and the lowest mobility ($15362 \text{ cm}^2 \text{ V}_s^{-1}$) belongs to the TNH even though it was grown at almost the optimum growth temperature for InGaAs alloy. After the annealing process, the electron mobility of high-temperature growth samples improved and almost became equal to the mobility of as-grown and annealed low-temperature growth sample's

electron mobility. It is evident that thermal annealing causes a slight improvement at all temperature ranges of interest for the low-temperature growth sample. After annealing, the low-temperature electron mobility is almost the same for both TNLB and TNHB samples. Therefore, it can be inferred that annealing has a significant effect for the high-temperature growth sample. The temperature-dependent carrier concentration changes of samples with and without annealing are shown in Figure 2b. Considering the TNH sample, a slight gradual increase in carrier concentration with increased temperature was observed where the highest value is recorded as $2.92 \times 10^{12} \text{ cm}^{-2}$ at 300K. After thermal annealing, we noted a decrease in carrier concentration to $2.4 \times 10^{12} \text{ cm}^{-2}$ at 300K.

To compare the effect of growth temperature and also thermal annealing on carrier mobility, analytical calculations of temperature-dependent mobility changes of as-grown and annealed samples are given in Figure 3 considering all possible scattering mechanisms. For all samples, the low-temperature electron mobility was restricted by alloy and interface roughness scattering mechanisms. Scattering caused by polar optical scattering dominates the mobility in the high-temperature samples. The interface roughness scattering resulted from two parameters, the lateral size ($\Delta=1.9a$ for TNH and $1.3a$ for TNLB) and the correlation length (Λ), which is used as adjustable parameters to fit the experimental data.

In addition, the alloy potential was used to determine the alloy disorder scattering mechanism. The values obtained are given in Table 1. with the values for the reference sample.

Table 1. Alloy potentials and correlation lengths for n-type $\text{In}_{0.32}\text{Ga}_{0.68}\text{As}/\text{GaAs}$ samples.

Sample	U_{Alloy} (eV)	(Λ) (nm)
TNL	0.445	1.3
TNLB	0.3	0.9
TNH	0.537	29.8
TNHB	0.487	0.7

The match between the experimental and calculated values for electron mobility was obtained at low temperatures for all samples, as given in Figure 3. The best match was obtained in the as-grown samples over all temperature ranges a slight deviation between experimental and calculated mobility was observed at temperatures higher than 77K. Also, increasing electron mobility was observed after annealing. From Figure 3, decreased contribution was observed for alloy disorder scattering and interface roughness scattering after thermal annealing. The optimum electronic transport properties, characterized by the lowest alloy potential and correlation length, were observed for the low-temperature growth sample. Following thermal annealing, the interface roughness was reduced for this sample. Since the mobility is lower for the sample grown at a higher temperature, thermal annealing is more effective in smoothing the interface.

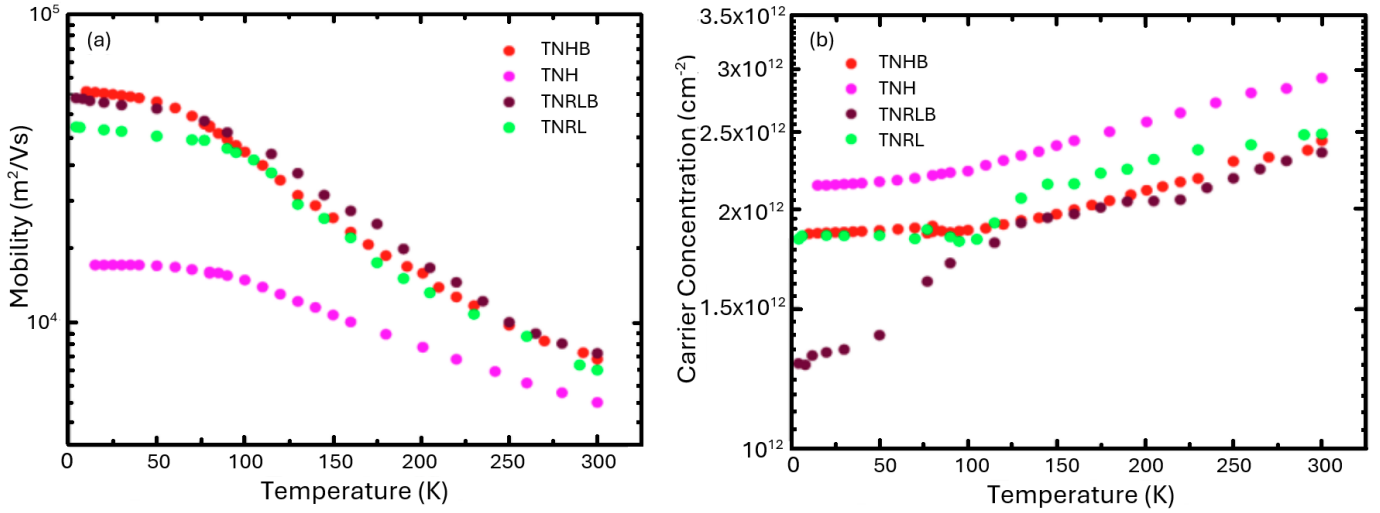


Figure 2. For all samples temperature-dependence of (a) Hall mobilities and (b) carrier concentrations.

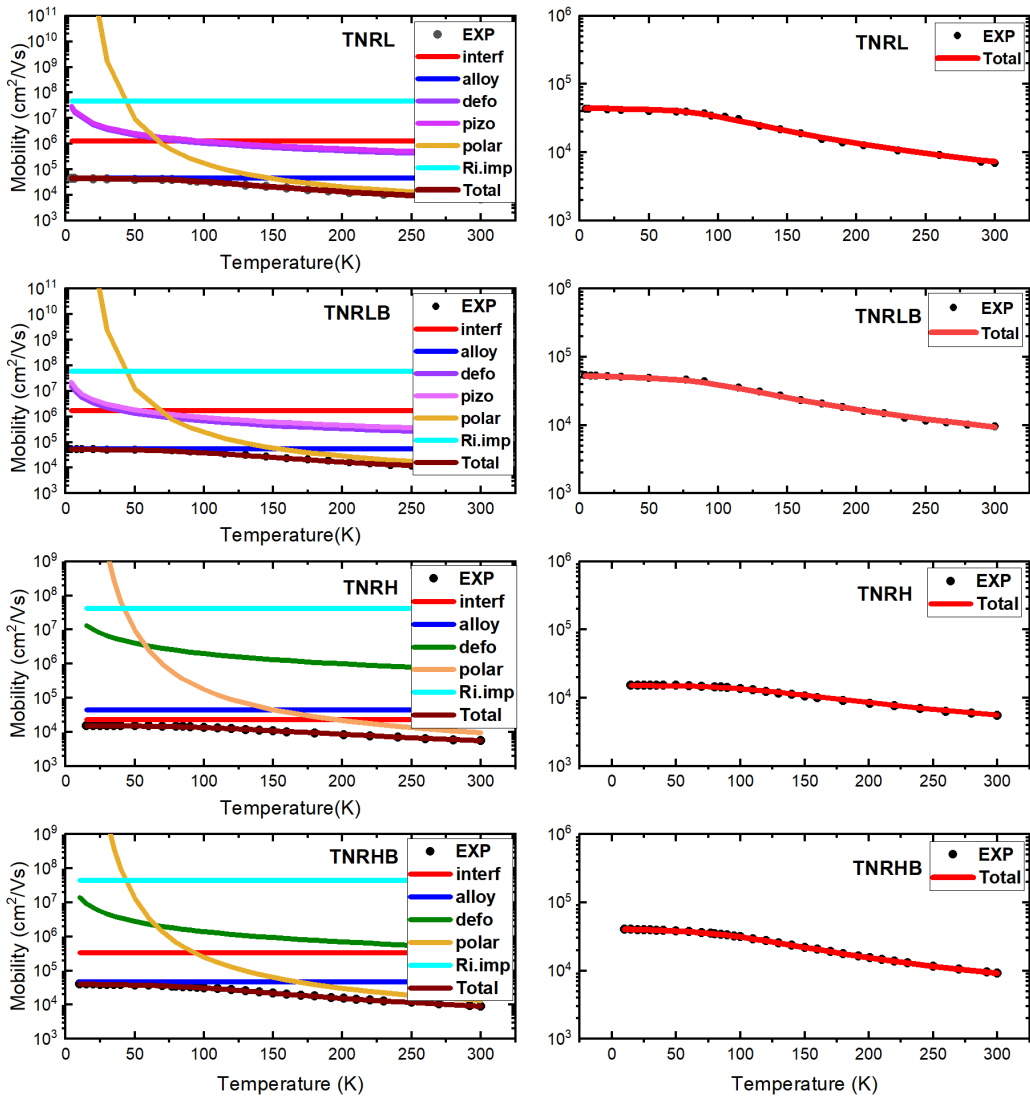


Figure 3. Analytical calculation of the temperature-dependent mobility of the samples.

Table 2. Variable parameters.

Parameters	Values
Optical phonon energy in GaInAs, $\hbar\omega_{po}$ (meV)	34
Optical phonon energy in GaAs, $\hbar\omega_{po}$ (meV)	35
Longitudinal acoustic phonon velocity, v_L (ms^{-1})	5087
Static dielectric constant, $\epsilon_s(\epsilon_0)$	13.9
High frequency dielectric constant, $\epsilon_\infty(\epsilon_0)$	11.11

Consequently, a significant enhancement was observed for the annealed high-temperature sample. Table 2 shows variable parameters used for calculation.

It has been reported that for In compositions greater than 0.2, InGaAs growth on GaAs results in In surface segregation at high-temperature growth. Thermal stability of InGaAs QW material requires low-temperature growth at around 400-500°C, but GaAs barrier material has to be grown at higher temperatures (around 580°C) (Toyoshima et al. 1993; Disseix et al. 1997). A strong temperature dependence of In segregation was revealed for InGaAs/GaAs QW structures with a segregation length of more than 30Å at temperatures above 600°C (Disseix et al. 1997). The surface segregation of In atoms drastically limits perfect abrupt interface between GaAs and InGaAs (Disseix et al. 1997). Despite several methods being used to solve this problem, the growth of high-quality InGaAs/GaAs QW structures remains a challenge. Therefore, we observed higher electron mobility for the sample grown at lower temperatures. However applying thermal annealing was found to be a solution to enhance mobility for high-temperature growth InGaAs/GaAs QW structures.

3.2. High Magnetic Field Results

MR measurements were carried out by sweeping the magnetic field value in the magnetic field range of 0-7T for TNL and TNLB samples and 0-18T for TNH and TNHB samples with different temperatures. SdH oscillations clearly appear at very low-magnetic fields due to the electron mobility values are so high for all samples as it can be seen in Figure 4. The MR curves for low-temperature growth as-grown (TNL) and annealed (TNLB) samples exhibit complicated characteristics, with both the period and shape of oscillations changing with increasing magnetic field. Experimentally observed magnetoresistance is the sum of classical magnetoresistance and SdH oscillations. To eliminate background magnetoresistance, the negative of the second derivative of the raw magnetoresistance data with respect to the magnetic field were taken, and are shown in Figure 5. The SdH oscillations in the second derivative of MR exhibit well-defined envelopes. As seen in Figure 4, the MR curve for high-temperature growth samples have a linearly increasing classical MR background with increasing magnetic field for the as-grown sample. For the annealed high temperature growth sample (TNHB), a slight deviation from linearity was observed above approximately 4T, while the

background MR characteristics exhibited linearity below 3.5T but deviated above 3.5T. Therefore, to be able to apply this second derivation method, only a low magnetic field range (<4T) was used for the samples apart from TNLB. As for TNLB, even at the low magnetic field range it was impossible to fit the oscillations using the standard expression given by Equation 14, but it is obtained well-defined SdH oscillations at higher magnetic field range, as seen in Figure 4b. However, the MR curves became more complicated at higher magnetic fields, as can be seen in Figure 4a, with an anomalous background MR. Even if the data is used to determine transport parameters of TNLB, it is clear these parameters cannot be compared with the transport parameters of other samples because they cannot be obtained at a similar magnetic field range. Effective electron mass values were obtained by proportioning the amplitudes of the SdH oscillations given in Figure 5 at a given magnetic field value and using Equation 17.

Figure 6 shows a plot of $\frac{1}{B}$ versus the peaks numbers for TNL and TNLB samples. Using the slopes of Figure 6 positions of Fermi level and N_{2D} (carrier concentration) for TNL and TNLB were obtained. All results obtained is given Table 3.

Table 3. Carrier density (N_{2D}), position of Fermi level and effective mass values obtained by analyzing SdH oscillations.

Sample	N_{2D} ($\times 10^{12} \text{ cm}^{-2}$)	$(E_F - E_i)$ (meV)	$m^*(m_0)$
TNL	1.74	71	0.057
TNLB	1.73	60	0.070
TNH	2.02	122	0.050
TNHB	1.92	82	0.055

4. CONCLUSION

Analysis of the temperature-dependent electron mobility showed that the 700°C thermal annealing had a significant improvement in the crystal structure. For the two samples grown at optimum and low growth temperature, the electronic properties of the sample at low growth temperature were superior in terms of electron mobility, alloy potential, and correlation length. Moreover, the post-growth thermal annealing at 700°C-600s improved the electronic properties of both samples at the growth temperature. According to the calculated transport parameters given in Table 3, the sample TNL had the lowest 2D carriers and the highest effective mass. Since the effective mass was larger, the density of states was higher, and therefore the Fermi level was smaller than those for TNH and TNHB samples. We exclude TNLB from the discussion because the analysis of this sample resulted in higher magnetic fields than the others. The 2D carrier density was the highest for TNH and the effective mass was the smallest, which resulted in the highest Fermi level. When the sample was annealed, 2D carrier density decreased and effective mass increased. The effective mass values became comparable for TNL and TNHB samples.

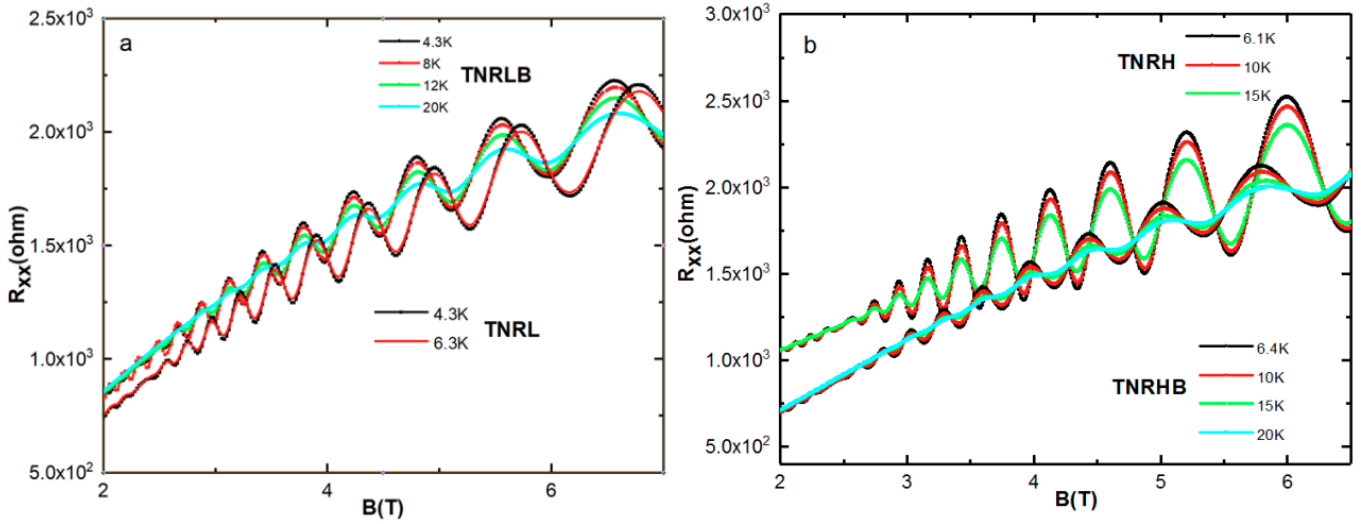


Figure 4. MR results of (a) TNL and TNLB, (b) TNH and TNHB.

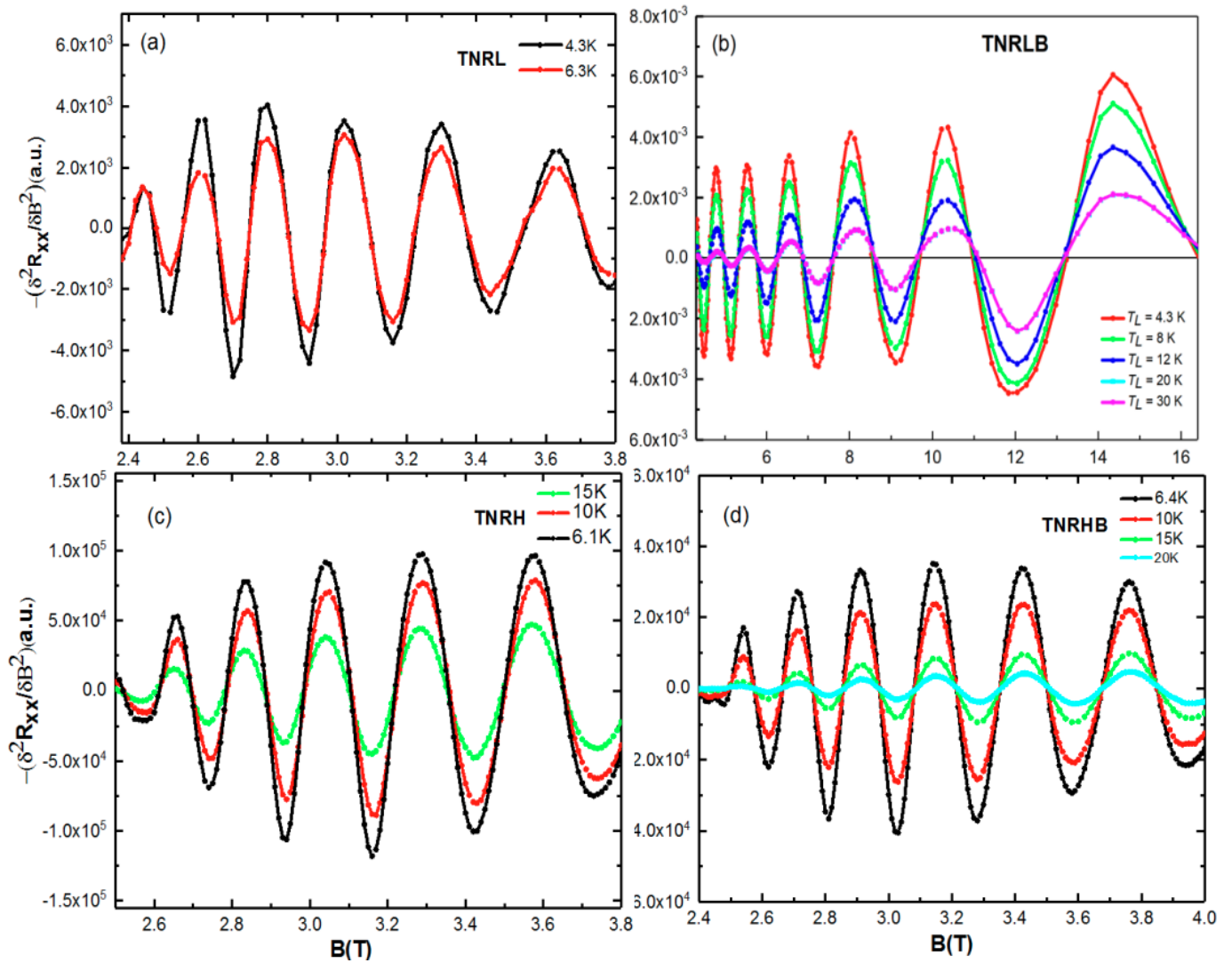


Figure 5. Negative second derivative of SdH oscillations for MR of (a) TNL, (b) TNLB, (c) TNH, and (d) TNHB.

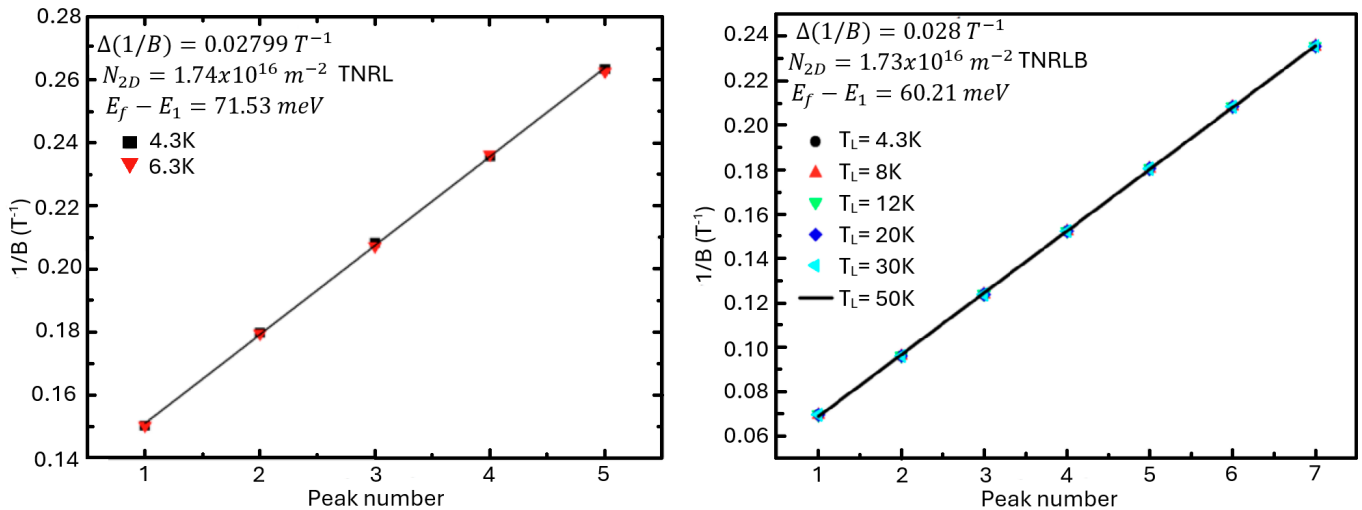


Figure 6. Plot of $1/B$ versus peak numbers for TNL (left panel) and TNLB (right panel).

The highest electron mobility for TNL sample was grown at a low temperature. The interface roughness for the TNL sample compared to the others was found to be the least. For all samples the alloy disorder scattering and interface roughness scattering were the prevailing scattering mechanisms. It was found that the alloy potential took a value of 0.445 eV for TNL and it was 0.537 eV for TNH. Following thermal annealing, an improvement in carrier mobility was observed. Additionally, a decrease in the correlation length was noted after the thermal annealing process, suggesting a reduction in interface roughness.

Peer Review: Externally peer-reviewed.

Author Contribution: Conception/Design of study - A.R., M.A., Ö.D., F.S., A.E.; Data Acquisition - A.R., M.A., Ö.D., F.S., A.E.; Data Analysis/Interpretation - A.R., M.A., Ö.D., F.S., A.E.; Drafting Manuscript - M.A., Ö.D., F.S., A.E.; Critical Revision of Manuscript - A.R., M.A., Ö.D., F.S., A.E.; Final Approval and Accountability - A.R., M.A., Ö.D., F.S., A.E.; Technical or Material Support - A.R., M.A., Ö.D., F.S., A.E.; Supervision - A.R., M.A., Ö.D., F.S., A.E.

Conflict of Interest: Authors declared no conflict of interest.

Financial Disclosure: This study was supported by the Scientific Research Projects Coordination Unit of Istanbul University (Project IDs: FBG-2022-38573, FBG-2021-37975, FBG-2018-30048).

LIST OF AUTHOR ORCIDS

A. Rajhi <https://orcid.org/0009-0009-1229-6965>
M. Aydın <https://orcid.org/0000-0002-1002-6007>
Ö. Dönmez <https://orcid.org/0000-0002-7635-3991>
F. Sarcan <https://orcid.org/0000-0002-8860-4321>
A. Erol <https://orcid.org/0000-0003-4196-1791>

REFERENCES

- Aldridge H., Lind A. G., Bomberger C. C., Puzyrev Y., Zide J. M., Pantelides S. T., Law M. E., Jones K. S., 2017, *Materials Science in Semiconductor Processing*, 62, 171
- Ardali S., Taganov S., Erol A., Tiras E., 2021, *Physica E: Low-Dimensional Systems and Nanostructures*, 125, 114344
- Balkan N., Çelik H., Vickers A. J., Cankurtaran M., 1995, *Physical Review B*, 52, 17210
- Coleridge P. T., 1990, *Semiconductor Science and Technology*, 5, 961
- Dahl D., 2002, *Solid State Communications*, 124, 825
- Disseix P., Leymarie J., Vasson A., Monier C., Grandjean N., Leroux M., Massies J., 1997, *Physical Review B - Condensed Matter and Materials Physics*, 55, 2406
- Donmez O., et al., 2014, *Semiconductor Science and Technology*, 29
- Donmez O., et al., 2020, *Semiconductor Science and Technology*, 35, 10
- Donmez O., et al., 2021, *Semiconductor Science and Technology*, 36, 11
- Feng G., Yoshimoto M., Oe K., Chayahara A., Horino Y., 2005, *Japanese Journal of Applied Physics, Part 2: Letters*, 44, 3
- Joncour M., Charasse M., Burgeat J., 1985, *Journal of Applied Physics*, 58, 3373
- Kosogov A. O., et al., 1996, *Applied Physics Letters*, 69, 3072
- Kuphal E., 1984, *Journal of Crystal Growth*, 67, 441
- Li W., et al., 2019, *Journal of Applied Physics*, 125
- Lin A., Doty M. F., Bryant G. W., 2019, *Phys. Rev. B*, 99, 075308
- Maspero R., Sweeney S. J., Florescu M., 2017, *Journal of Physics Condensed Matter*, 29, 075001
- Matthews J. W., Blakeslee A., 1974, *Journal of Crystal Growth*, 27, 118
- Muraki K., Fukatsu S., Shiraki Y., Ito R., 1992, *Applied Physics Letters*, 61, 557
- Petropoulos J. P., Zhong Y., Zide J. M., 2011, *Applied Physics Letters*, 99
- Toyoshima H., Niwa T., Yamazaki J., Okamoto A., 1993, *Applied Physics Letters*, 63, 821
- Zanato D., Gokden S., Balkan N., Ridley B. K., Schaff W. J., 2004, *Semiconductor Science and Technology*, 19, 427